

The pulsar gamma-ray emission from the high-resolution dissipative magnetospheres

GANG CAO¹ AND XIONGBANG YANG¹

¹*Department of Mathematics, Yunnan University of Finance and Economics, Kunming 650221, Yunnan, P. R. China, gcao@ynufe.edu.cn*

ABSTRACT

The pulsar light curves and energy spectra are explored in dissipative pulsar magnetospheres with the Aristotelian electrodynamics (AE), where particle acceleration is fully balanced with radiation reaction. The AE magnetospheres with non-zero pair multiplicity are computed by a pseudo-spectral method in the co-moving frame. The dissipative region near the current sheet outside the LC is accurately captured by the high-resolution simulation. The pulsar light curves and spectra are computed by the test particle trajectory method including the influence of both the consistent accelerating electric field and radiation reaction. Our results can generally reproduce the double-peak light curves and the GeV cut-off energy spectra in agreement with the Fermi observations for the pair multiplicity $\kappa \gtrsim 1$.

Keywords: magnetic field - method: numerical - gamma-ray: star - pulsars: general

1. INTRODUCTION

The Fermi Gamma-Ray Space Telescope launched in 2008 has opened a new era on the study of pulsar γ -ray emission. To date, the Fermi LAT have detected more than 270 γ -ray pulsars¹, 117 of which are listed in the Second Fermi Pulsar Catalog (Abdo et al. 2010, 2013). Fermi γ -ray pulsars are classified into three groups: young radio-loud, young radio-quiet and millisecond pulsars. The light curves from these pulsars usually show the widely separated double-peak profiles, and the first peak lags the radio peak by a small fraction of rotation period. The pulsar γ -ray spectra can be described by a power law with an exponential cut-off, and the cut-off energy is in the range of 1-5 GeV. The light curves and energy spectra from the Fermi LAT offer a unique insight to explore the nature of the radiation mechanisms and the location of particle acceleration in the magnetosphere. However, it is still uncertain about the origin of pulsar emission. In fact, the pulsed emission and particle acceleration in the magnetosphere are controlled by the structure of the global pulsar magnetosphere. This requires us to have a deep and accurate knowledge of the pulsar magnetosphere. The significant progresses have been made in the numerical model of the global pulsar magnetospheres within the last decades.

It is well believed that the pulsar magnetosphere is loaded with plasmas by pair creation (Goldreich & Julian 1969). A zeroth order approximation of the plasma-

filled magnetosphere is referred to the force-free electrodynamics (FFE). The force-free approximation requires the density number much larger than GJ density, these plasmas quickly short out the accelerating fields so that the force-free condition $\mathbf{E} \cdot \mathbf{B} = 0$ holds everywhere. The force-free pulsar magnetosphere have been recently achieved with the advent of numerical simulations. The numerical force-free solution is firstly obtained by Contopoulos et al. (1999, hereafter CKF) for the aligned rotator and then by Spitkovsky (2006) for the oblique rotator. 3D force-free solutions are further explored by the finite-difference time-domain method (Kalapotharakos & Contopoulos 2009; Contopoulos & Kalapotharakos 2010) and the spectral method (Pétri 2012; Cao et al. 2016b; Pétri 2016). All these time-dependent force-free simulations confirmed the existence of the current sheet outside the LC, which is thought as the potential site of the pulsar γ -ray emission. The pulsar light curves and spectra are also studied by placing the emission region in the current sheet outside the LC (Bai & Spitkovsky 2010; Harding & Kalapotharakos 2015; Brambilla et al. 2015; Bogovalov et al. 2018; Harding et al. 2018). However, the force-free solution do not allow any particle acceleration and production of the pulsed radiation in the magnetosphere.

More realistic pulsar model should allow the local dissipation to produce the observed pulsar phenomenons. The dissipative effects have been included by involving a finite conductivity (Li et al. 2012; Kalapotharakos et al. 2012a; Cao et al. 2016b), which is called the resistive magnetosphere. The resistive magnetosphere ranges from the vacuum limit to force-free limit with

¹ <https://confluence.slac.stanford.edu/display/GLAMCOG/Public+List+of+LAT-Detected+Gamma-Ray+Pulsars>

increasing conductivity, and the resistive solution produces accelerating electric fields that are self-consistent with the magnetic field structure. The resistive magnetospheres have been used to model the pulsar light curves (Kalapotharakos et al. 2012b, 2014, 2017; Cao & Yang 2019) and energy spectra (Yang & Cao 2021) by including the accelerating electric field from the simulation. These studies suggested that the particle acceleration and the γ -ray radiation is produced near the current sheets outside the LC. Recently, particle-in-cell (PIC) methods are developed to model the pulsar magnetosphere by self-consistently treating the feedback between particle motions and the electromagnetic fields (Philippov & Spitkovsky 2014; Chen & Beloborodov 2014; Philippov et al. 2015; Belyaev 2015; Cerutti et al. 2015; Kalapotharakos et al. 2018; Brambilla et al. 2018). Moreover, the pulsar light curves are predicted by extracting particle radiation along each trajectory in full PIC simulation (Cerutti et al. 2016; Philippov & Spitkovsky 2018; Kalapotharakos et al. 2018). However, the particle energy from the PIC simulation are much small than those in the real pulsar, which is not enough to produce the observed Fermi γ -ray emission.

A good approximation between the resistive model and PIC model is Aristotelian electrodynamics, which can include the back-reaction of the emitting photons onto particle motions and allow for some dissipations in the magnetosphere. The AE method is firstly introduced to study the pulsar magnetosphere by Gruzinov (2012, 2013). Recently, a clever method by combining FFE with AE is proposed to construct the structure of pulsar magnetosphere (Contopoulos et al. 2016; Pétri 2020a; Cao & Yang 2020). Contopoulos et al. (2016) first presented the 3D structure of the AE magnetosphere for the oblique rotator by the finite-difference method. However, they only studied the AE solution in the limit of no pair multiplicity. Pétri (2020a) extended the study of Contopoulos et al. (2016) by introducing non-zero pair multiplicity and used the spectral method to compute the AE magnetosphere but only for the aligned rotator. Recently, Cao & Yang (2020) presented the first AE solution with non-zero pair multiplicity for the oblique rotator by the spectral method. They show that the dissipative region is more restricted to the current sheet outside LC as the pair multiplicity increases. However, a relatively low resolution is generally used in all these simulations, which is not enough to accurately capture the current sheet outside the LC. Moreover, the light curves and spectra were not computed from the numerical AE solutions in all these studies. In this paper, we present the high-resolution simu-

lation of the AE magnetosphere with non-zero pair multiplicity for the oblique rotator by the spectral method. The pulsar light curves and spectra are then computed by the test particle trajectory method in dissipative AE magnetosphere. The paper is organized as follows: We describe the AE model in section 2. We present the pulsar light curves and spectra from the AE magnetosphere in section 3. A brief discussion and conclusions are presented in section 4.

2. ARISTOTELIAN ELECTRODYNAMICS

It is difficult to determine whether the magnetosphere has reached a steady state at the end of the simulation, especially for the oblique rotator in which all the field lines remain time-dependent in the observer frame. Therefore, it is useful to study the pulsar magnetosphere for stationary state in the co-moving frame, in which the magnetosphere relaxes to the time-independent solution where all the field lines remain time-independent. The time-dependent Maxwell equations in the co-moving frame are given by (Muslimov & Harding 2005; Pétri 2020b)

$$\frac{\partial \mathbf{B}}{\partial t'} = -\nabla \times (\mathbf{E} + \mathbf{V}_{\text{rot}} \times \mathbf{B}), \quad (1)$$

$$\frac{\partial \mathbf{E}}{\partial t'} = \nabla \times (\mathbf{B} - \mathbf{V}_{\text{rot}} \times \mathbf{E}) - \mathbf{J} + \mathbf{V}_{\text{rot}} \nabla \cdot \mathbf{E}, \quad (2)$$

$$\nabla \cdot \mathbf{B} = 0, \quad (3)$$

$$\nabla \cdot \mathbf{E} = \rho_e, \quad (4)$$

where ρ_e and \mathbf{J} is the charge density and the current density, respectively. It is noted that \mathbf{E} and \mathbf{B} are still defined in the observed frame. The pulsar magnetosphere can be computed by implementing a prescription for the current density \mathbf{J} .

The pulsar magnetosphere cannot be surrounded by vacuum, because the rotating vacuum solution produces an accelerating electric field which is able to extract the particles from the stellar surface and fill the magnetosphere. Therefore, the realistic pulsar magnetospheres require the presence of plasma and have some dissipation regions to produce the particle acceleration and the pulsed radiation. The emitted photon has a back-reaction onto the particle motion in a direction opposite to its motion. This process can be easily treated by assuming a stationary balance between the particle acceleration and radiation, which is called Aristotelian electrodynamics. The current density in the AE magnetosphere can be defined by introducing the pair multiplicity κ as (Cao & Yang 2020)

$$\mathbf{J} = \rho_e \frac{\mathbf{E} \times \mathbf{B}}{B^2 + E_0^2} + (1 + \kappa) |\rho_e| \frac{(B_0 \mathbf{B} + E_0 \mathbf{E})}{B^2 + E_0^2}. \quad (5)$$

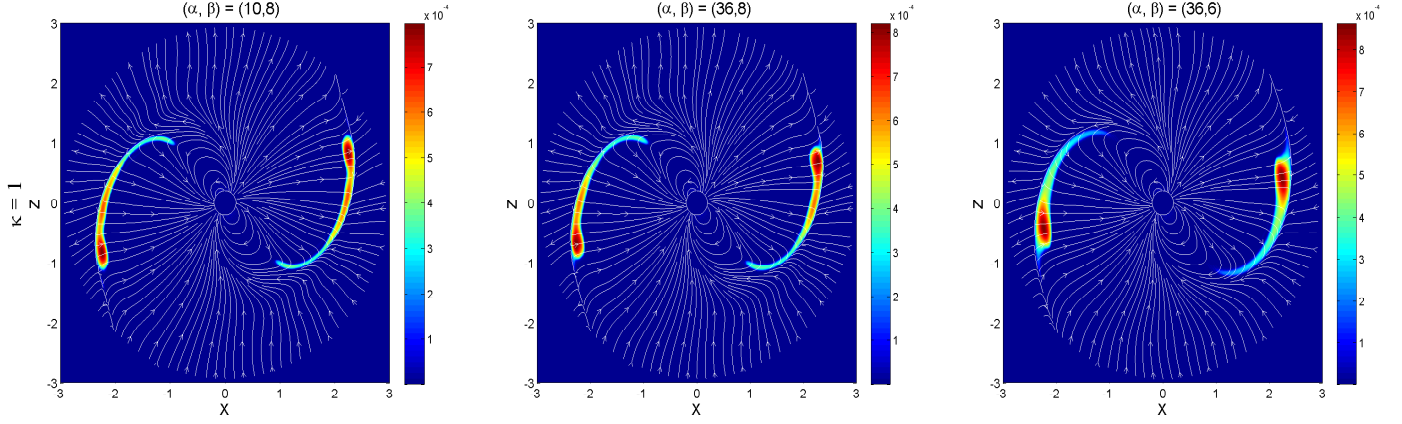


Figure 1. Distribution of the magnetic field lines and the accelerating electric field E_0 in the x - z plane for a $\alpha = 60^\circ$ dissipative rotator with the pair multiplicity $\kappa = 1$ by using different filter parameters, where E_0 is the unit of the stellar surface magnetic field.

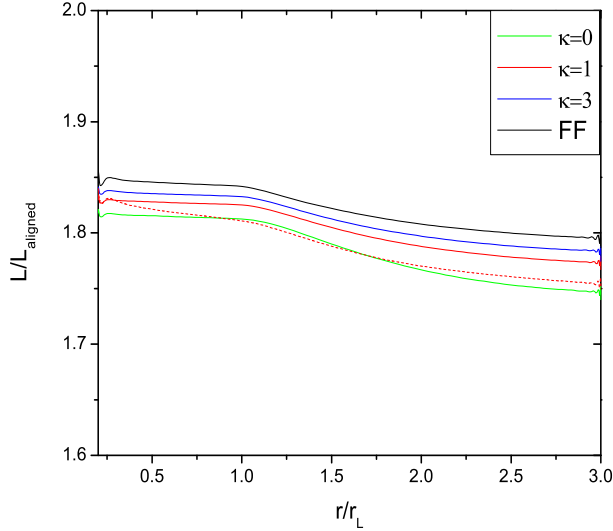


Figure 2. The normalized Poynting flux L/L_{aligned} as a function of radius r for a $\alpha = 60^\circ$ dissipative rotator with different pair multiplicities κ . The red dashed curve is the normalized Poynting flux with the pair multiplicity $\kappa = 1$ for the low resolution of $N_r \times N_\theta \times N_\phi = 129 \times 32 \times 64$ and the same optimized filtering parameter of $(\alpha, \beta) = (10, 8)$.

where B_0 and E_0 are the magnetic and electric field in the frame in which \mathbf{E} and \mathbf{B} are parallel. The quantities B_0 and E_0 is given by the relations

$$B_0^2 - E_0^2 = \mathbf{B}^2 - \mathbf{E}^2, \quad (6)$$

$$E_0 B_0 = \mathbf{E} \cdot \mathbf{B}, \quad (7)$$

with $E_0 \geq 0$.

The force-free approximation satisfies the force-free condition $\mathbf{E} \cdot \mathbf{B} = 0$ and requires the condition $E \leq B$ in the whole magnetosphere. The current sheet is captured by enforcing the condition $E = B$ in the regions where $E > B$. Therefore, the force-free approximation can not

produce any dissipative regions where $E > B$. However, the AE model can allow for dissipation in some regions where $E > B$. It is well known that the pulsar magnetosphere should allow for a local dissipation to produce the pulsed emission. The recent numerical simulations shown that the current sheet is a promising site for particle acceleration and high-energy radiation in the magnetosphere. To explore the dissipation where $E > B$, we use the force-free description where $E \leq B$ and the AE description where $E > B$. It is expected that our model will produce the dissipative region with $E > B$ outside the LC.

3. RESULT

3.1. Magnetospheric Structure

The time-dependent Maxwell equations are solved by a spectral algorithm in the co-moving frame with the combined FFE and AE description. The electromagnetic field are discretized by a set of the spectral collocation points in spherical coordinates (r, θ, ϕ) . The radial components of the electromagnetic field are expanded onto the Chebyshev polynomial, and the angle components are expanded onto the vector spherical harmonic expansion. We improve the time-integration described in Cao & Yang (2020) by using a combined three-order Runge-Kutta and Adam-Bashforth method. An exponential filter with $\sigma(\eta) = \exp(-\alpha \eta^\beta)$ in all directions is used to smooth the electromagnetic field at each time step. The divergenceless condition on the magnetic field is analytically enforced by a projection method. The simulation is initialized with a dipole magnetic field and a zero electric field outside the star. We enforce the inner boundary condition at the stellar surface with a rotating electric field $\mathbf{E} = -(\boldsymbol{\Omega} \times \mathbf{r}) \times \mathbf{B}/c$. We use a non-reflecting boundary condition to prevent

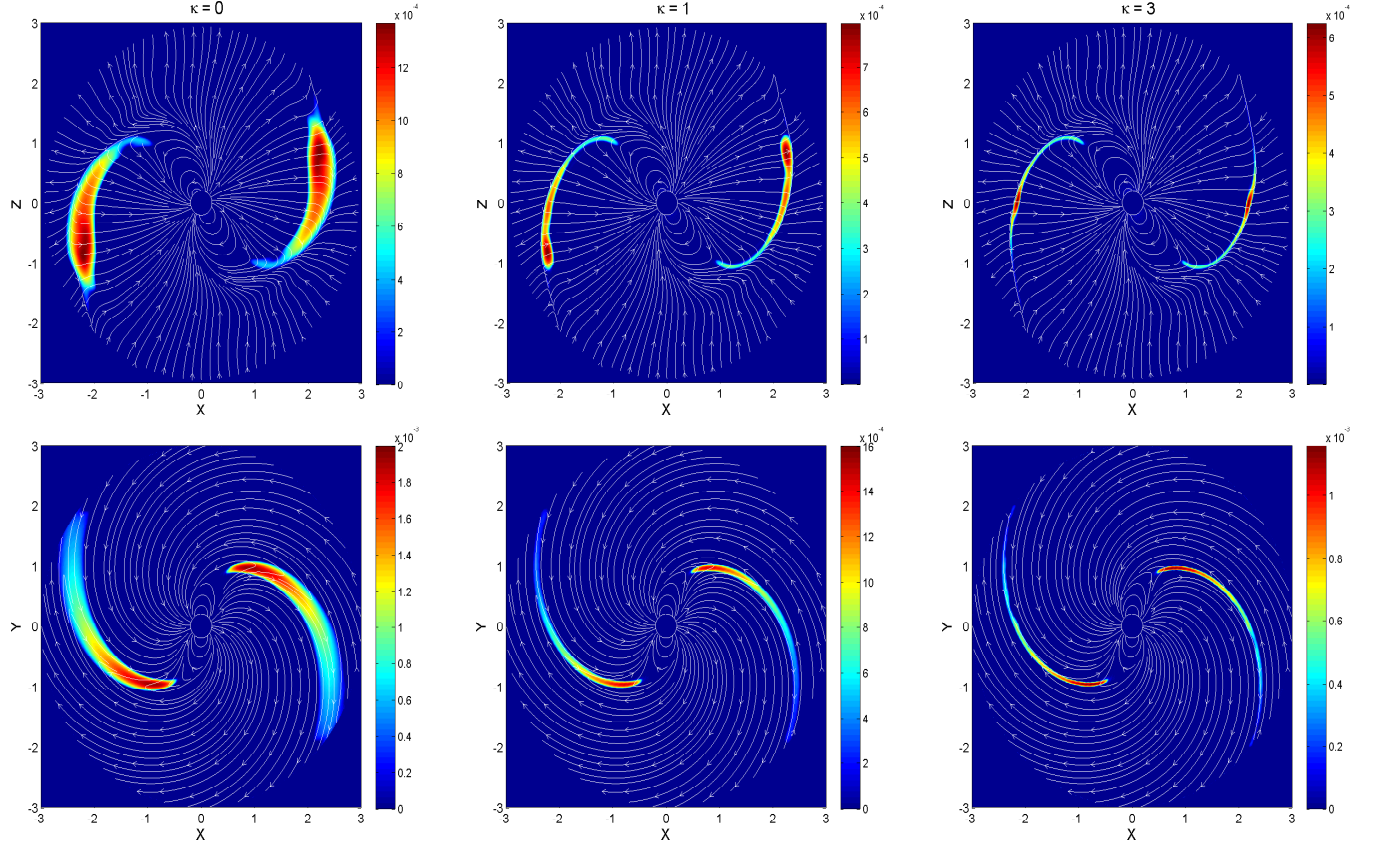


Figure 3. Distribution of the magnetic field lines and the accelerating electric field E_0 for a $\alpha = 60^\circ$ dissipative rotator with the pair multiplicity $\kappa = \{0, 1, 3\}$ and the optimized filtering parameters $(\alpha, \beta) = (10, 8)$ in the x - z plane (the top plane) and in the x - y plane (the bottom plane), where E_0 is the unit of the stellar surface magnetic field.

reflection from the outer boundary. The simulation domain is set to $r \in (0.2 - 3) r_L$. A high resolution with $N_r \times N_\theta \times N_\phi = 129 \times 64 \times 128$ is used to catch the current sheet in all simulations. We performed several simulations for magnetic inclination angle $\chi = \{0^\circ, 15^\circ, 30^\circ, 45^\circ, 60^\circ, 75^\circ, 90^\circ\}$ with the pair multiplicity $\kappa = \{0, 1, 3\}$. The system is evolved for several rotational periods to ensure that a steady solution has been reached.

A spectral filter is necessary to prevent Gibbs oscillation and non-linear instabilities in the spectral algorithm. A non-physical dissipation is introduced by the filtering processes. It is difficult to correctly catch the discontinuity induced by the current sheet, which can be circumvent by increasing simulation resolution and adjusting the spectral filter. We show the distribution of the magnetic field line and the accelerating electric field E_0 in the x - z plane for a 60° rotator with the pair multiplicity $\kappa = 1$ by using different filter parameters in figure 1. We see that all solutions have similar E_0 distributions in the current sheet, they are independent of the choice of a filter as it should be. A low-order

filter with $(\alpha, \beta) = (10, 6)$ gives more dissipation solution with large numerical diffusion in the current sheet than a high-order filter with $(\alpha, \beta) = (10, 8)$ and $(\alpha, \beta) = (36, 8)$. A more accurate solution can be obtained by using a optimized filtering parameter $(\alpha, \beta) = (10, 8)$ with a high-order filter and a suitable α value. The normalized Poynting flux L/L_{aligned} as a function of radius r for a 60° rotator with different pair multiplicities are shown in figure 2. For comparison, we also show the normalized Poynting flux with the pair multiplicity $\kappa = 1$ for the low-resolution simulation and the same optimized filtering parameter as the red dashed line. It is found that the Poynting flux increases with increasing κ values and approaches the force-free solution for the high κ value. It is expected that there is no dissipation inside the LC in the combined FFE and AE magnetosphere. We see that the high-resolution simulation show smaller dissipation in the LC compared to the low-resolution simulation. Our simulation show that the dissipative region in the current sheet can be better resolved by both increasing the grid resolution and controlling the filtering effect in our spectral algorithm. It is noted that

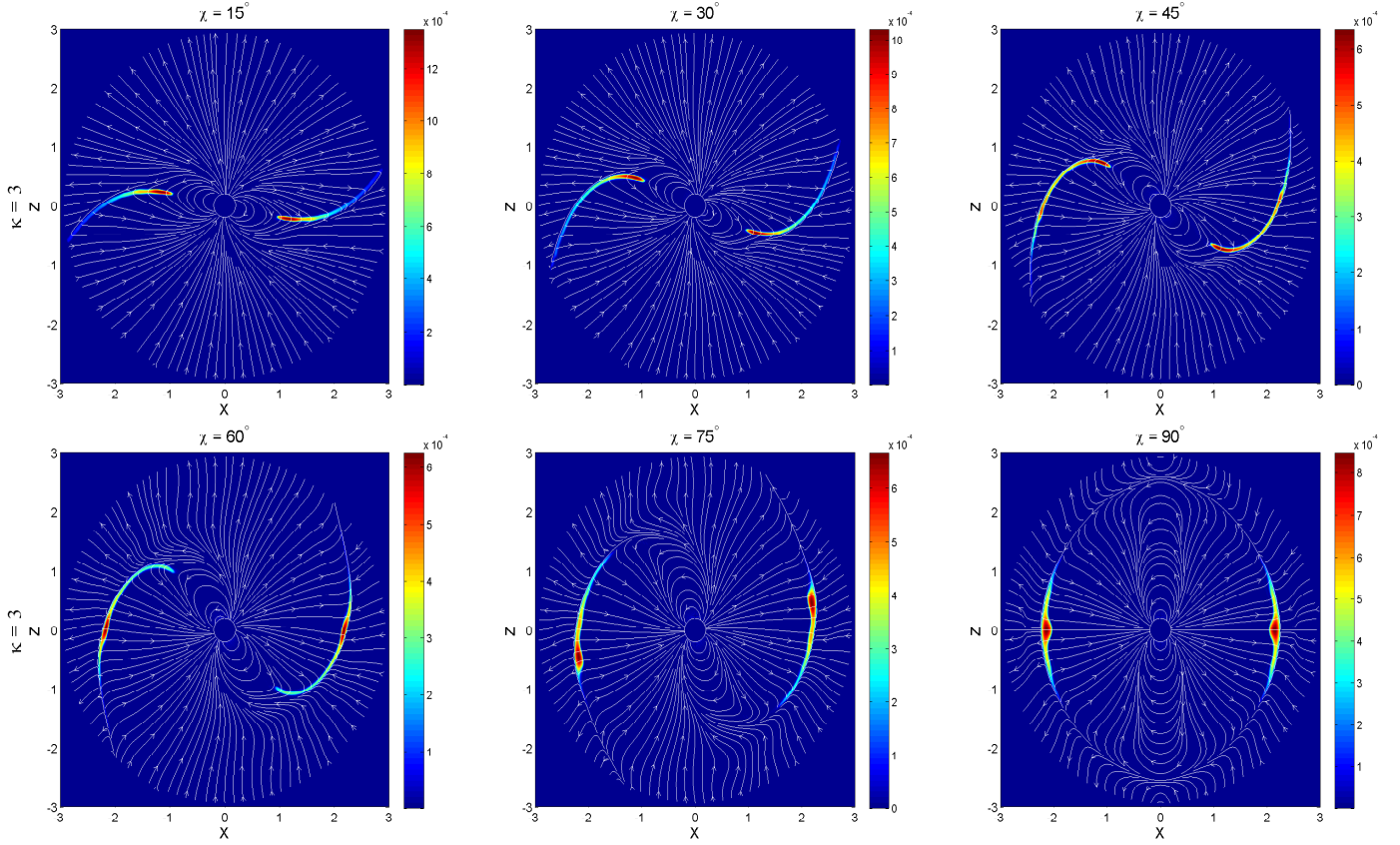


Figure 4. Distributions of the magnetic field lines and the accelerating electric field E_0 for different magnetic inclination angles with the pair multiplicity $\kappa = 3$ in the x - z plane, where E_0 is the unit of the stellar surface magnetic field.

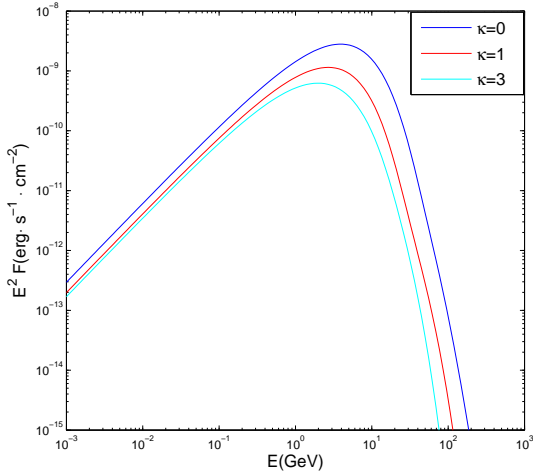


Figure 5. The curvature radiation spectra for a 60° magnetosphere with the pair multiplicities $\kappa = \{0, 1, 3\}$.

the low-resolution simulation and/or the high-resolution simulation with the strong spectral filter show more dissipative accelerating regions in the current sheet, which produces the higher cut-off energy in the curvature radiation spectrum.

We show the distribution of the magnetic field line and the accelerating electric field E_0 for a 60° rotator with the pair multiplicity $\kappa = \{0, 1, 3\}$ and the optimized filtering parameters $(\alpha, \beta) = (10, 8)$ in the x - z and x - y plane in figure 3. As the pair multiplicity κ increases, the magnetosphere tends to the force-free solution with a current sheet outside the LC. We observe a strong E_0 region with $E > B$ outside the LC. The dissipative region decreases with increasing pair multiplicity and the dissipative region are more confined to near the current sheet outside the LC for high pair multiplicity. We also show the distribution of the magnetic field line and the accelerating electric field E_0 for different inclination angles with the pair multiplicity $\kappa = 3$ in the x - z plane in figure 4. We see that all solutions have a near force-free magnetosphere with the dissipative region only near the current sheet for all the inclination angles. Our high-resolution simulation with the optimized filtering parameter gives more accurate solution near the current sheet compared to those in Cao & Yang (2020) and Pétri (2020b).

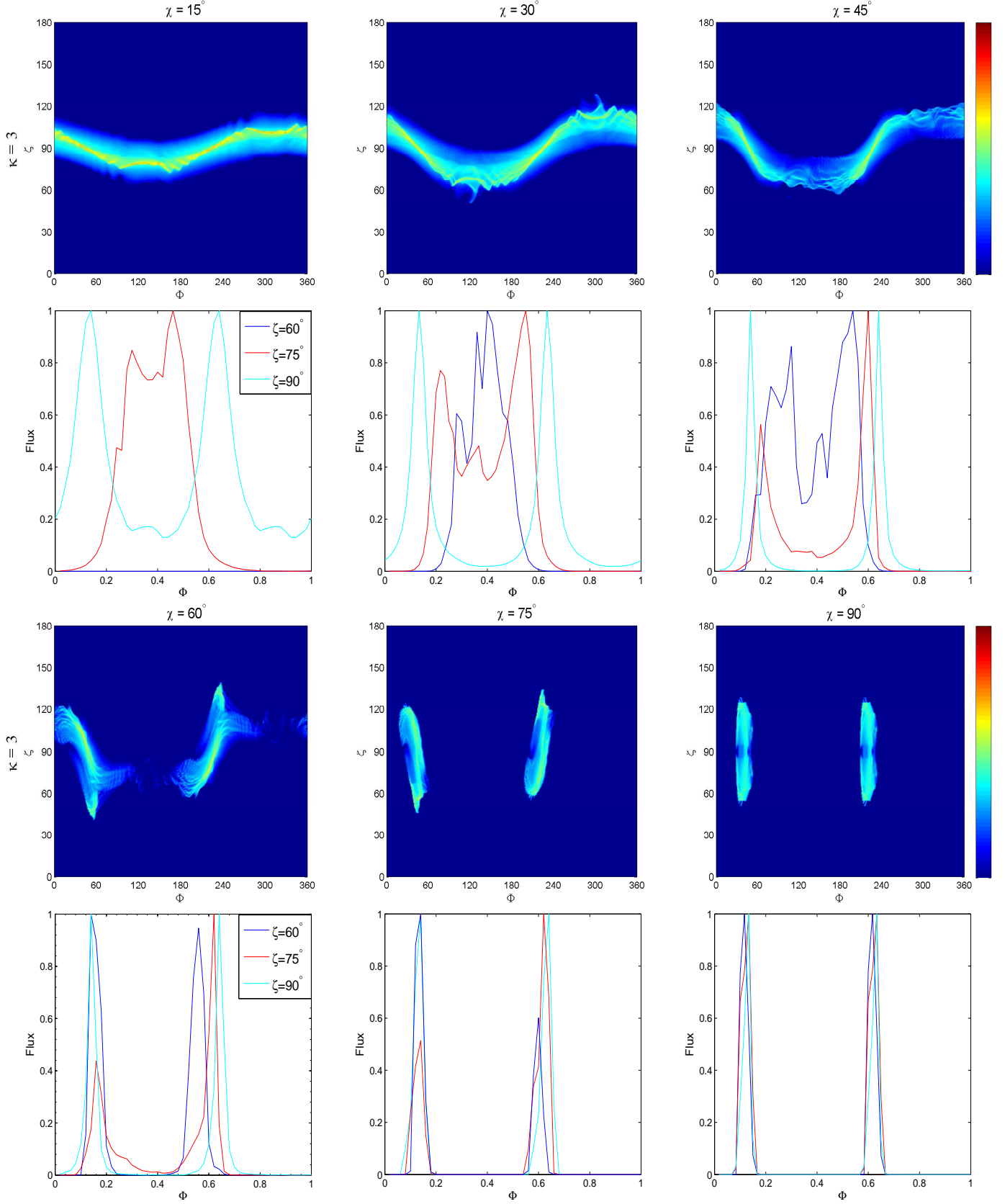


Figure 6. The sky maps and the corresponding light curves at > 1 GeV energies in different inclination angles and view angles with the pair multiplicity $\kappa = 3$.

3.2. Light curves and energy spectra

The particle velocity in the radiation reaction limit is defined by (Gruzinov 2012, 2013)

$$\mathbf{v}_{\pm} = \frac{\mathbf{E} \times \mathbf{B} \pm (B_0 \mathbf{B} + E_0 \mathbf{E})}{B^2 + E_0^2}, \quad (8)$$

where the two signs correspond to positrons and electrons, they have a different way to radiation reaction in the AE magnetosphere. The Lorentz factor along particle trajectory is given by

$$\frac{d\gamma}{dt} = \frac{q_e c E_0}{m_e c^2} - \frac{2q_e^2 \gamma^4}{3R_{\text{CR}}^2 m_e c}, \quad (9)$$

The energy spectrum of curvature radiation for each particle with Lorentz factor γ is given

$$F(E_\gamma, r) = \frac{\sqrt{3}e^2\gamma}{2\pi\hbar R_{\text{CR}}} F(x), \quad (10)$$

where $x = E_\gamma/E_{\text{cur}}$, E_γ is the radiation photon energy, $E_{\text{cur}} = \frac{3}{2}c\hbar\frac{\gamma^3}{R_{\text{CR}}}$ is the characteristic energy of the curvature radiation photon, R_{CR} is the curvature radius of particles, and the function $F(x)$ is defined as

$$F(x) = x \int_x^\infty K_{5/3}(\xi) d\xi, \quad (11)$$

The initial particles are randomly injected from the polar caps on the stellar surface with small Lorentz factor. The particle trajectory is determined by integrating the particle velocity from the neutron star surface up to $r = 2.5 r_L$. The Lorentz factor along each trajectory is then computed under the influence of the local accelerating electric field and the curvature radiation loss. Assuming that the direction of the photon emission is along the direction of particle motion, we can compute the direction of the photon emission and the curvature radiation spectrum along each trajectory. The pulsar light curves and spectra can be constructed by collecting all curvature radiation photons from each radiating particle in sky maps.

We show the curvature radiation spectra for a 60° magnetosphere with different pair multiplicity $\kappa = \{0, 1, 3\}$ in figure 5. It can be seen that our model can produce a power-law spectrum with an exponential cut-off. Moreover, the cut-off energy decreases as the pair multiplicity κ increases, which is caused by the decrease of the accelerating electric field in the dissipative region outside the LC. We also find that the cut-off energy lies in the range of 1-5 GeV for the pair multiplicity $\kappa \gtrsim 1$, which is consistent with the Fermi observed GeV cut-off energy. We also find that the spectra for all the inclination angles are very similar to those presented in

Figure 5. We show the sky maps and the corresponding light curves in different inclination angles and view angles with the pair multiplicity $\kappa = 3$ in figure 6. We see that the double-peak light curves can generally be produced for a broad range of the inclination angles and view angles, which are generally agreement with those observed by Fermi-LAT. Our results support that the observed γ -ray pulsar population is consistent with curvature radiation (Kalapotharakos et al. 2019).

4. DISCUSSION AND CONCLUSIONS

We firstly explore the properties of the pulsar light curves and energy spectra in dissipative AE magnetospheres. The dissipative AE magnetospheres with non-zero pair multiplicity are presented by a pseudo-spectral method with the high-resolution simulations in the co-moving frame. Our simulations show that the dissipative region near the current sheet outside the LC can be accurately captured by the high-resolution simulation. We use these field structures to define the trajectory of the positron and electron with the radiation reaction. The pulsar light curves and energy spectra are then produced by collecting all curvature radiation photons along each particle trajectory. Our results show that the double-peak light curves and the power-law energy spectra with an exponential cut-off at ~ 1 GeV energy range can generally be produced for a moderate pair multiplicity $\kappa \gtrsim 1$, which are well consistent with those observed by Fermi-LAT.

Our study provide the first step to model the pulsar emission for direct comparison with observation by including consistent accelerating electric field and radiation reaction from the dissipative AE magnetosphere. It is necessary to perform more magnetosphere simulations with a broader range of the magnetic inclination and the pair multiplicity to construct the pulsar light curves and spectra, which allow us directly compare them with the Fermi observations. This comparison will provide the meaningful constraints on the model parameters and enhance our understanding about the physical mechanisms of pulsar gamma-ray emission. We will present the detailed comparisons with the Fermi observational data in the near future.

ACKNOWLEDGMENTS

We thank the anonymous referee for valuable comments and suggestions. We would like to thank Jérôme Pétri and Ioannis Contopoulos for some useful discussions. We acknowledge the financial support from the National Natural Science Foundation of China 12003026, and the Basic research Program of Yunnan Province 202001AU070070.

REFERENCES

- Abdo, A. A., Ackermann, M., Ajello, M., et al. 2010, *ApJS*, 187, 460
- Abdo, A. A., Ajello, M., Allafort, A., et al. 2013, *ApJS*, 208, 17
- Bai, X.N., & Spitkovsky, A. 2010, *ApJ*, 715, 1282
- Belyaev, M. A. 2015, *MNRAS*, 449, 2759
- Brambilla, G., Harding, A. K., Kalapotharakos, K., & Kazanas, D. 2015, *ApJ*, 804, 84
- Brambilla, G., Kalapotharakos, K., Timokhin, A. N., Harding, A. K., & Kazanas, D. 2018, *ApJ*, 858, 81
- Bogovalov, S. V., Contopoulos, I., Prosekin, A., Tronin, I., & Aharonian, F. A. 2018, *MNRAS*, 476, 4213
- Cao, G., Zhang, L., & Sun, S. N. 2016a, *MNRAS*, 455, 4267.
- Cao, G., Zhang, L., & Sun, S. N. 2016b, *MNRAS*, 461, 1068.
- Cao, G., & Yang, X. B. 2019, *ApJ*, 874, 166
- Cao, G., & Yang, X. B. 2020, *ApJ*, 889, 29
- Chen, A. Y., & Beloborodov A. M. 2014, *ApJ*, 795, L22
- Contopoulos, I., Kazanas, D., & Fendt, C. 1999, *ApJ*, 511, 351
- Contopoulos, I., & Kalapotharakos, C. 2010, *MNRAS*, 404, 767
- Contopoulos I. 2016, *MNRAS*, 463, L94
- Cerutti, B., Philippov, A., Parfrey, K., & Spitkovsky, A. 2015, *MNRAS*, 448, 606
- Cerutti B., Philippov A. A., & Spitkovsky, A. 2016, *MNRAS*, 457, 2401
- Goldreich, P., & Julian, W. H. 1969, *ApJ*, 157, 869
- Gruzinov, A. 2012, arXiv: 1205.3367
- Gruzinov, A. 2013, arXiv:1303.4094
- Harding, A. K., & Kalapotharakos, C. 2015, *ApJ*, 811, 63
- Harding, A. K., Kalapotharakos, C., Barnard, M., & Venter, C. 2018, *ApJ*, 869, L18
- Kalapotharakos, C., & Contopoulos, I. 2009, *A&A*, 496, 495
- Kalapotharakos, C., Kazanas D., Harding, A., & Contopoulos, I. 2012a, *ApJ*, 749, 2
- Kalapotharakos, C., Harding, A. K., Kazanas, D., & Contopoulos, I. 2012b, *ApJL*, 754, L1
- Kalapotharakos, C., Harding, A. K., & Kazanas, D. 2014, *ApJ*, 793, 97
- Kalapotharakos, C., Harding, A. K., Kazanas, D., & Brambilla, G. 2017, *ApJ*, 842, 80
- Kalapotharakos, C., Brambilla, G., Timokhin, A., Harding, A. K., & Kazanas, D. 2018, *ApJ*, 857, 44
- Kalapotharakos, C., Harding, A. K., Kazanas, D., & Wadiasingh, Z. 2019, *ApJL*, 883, L4
- Li, J., Spitkovsky, A., & Tchekhovskoy, A. 2012, *ApJ*, 746, 60
- Muslimov, A. G., & Harding, A. K. 2005, *ApJ*, 630, 454
- Philippov, A. A., & Spitkovsky, A. 2014, *ApJ*, 785, L33
- Philippov, A. A., Spitkovsky, A., & Cerutti, B. 2015, *ApJ*, 801, L19
- Philippov, A. A., & Spitkovsky, A. 2018, *ApJ*, 855, 94
- Pétri, J. 2012, *MNRAS*, 424, 605
- Pétri, J. 2016, *MNRAS*, 455, 3779
- Pétri, J. 2019, *MNRAS*, 484, 5669
- Pétri, J. 2020, *Universe*, 6, 15
- Spitkovsky, A. 2006, *ApJ*, 648, L51
- Yang, X. B., & Cao, G. 2021, *ApJ*, 909, 88